metals

MDPI

Article

Static Recrystallization Behavior and Microstructure Evolution of SA-508M Gr.3 Steel

Chuang Mao [1], Mingze Liu [2], Lanjun Ren [3], Xinrui Wang [2], Lei Sun [1], Jinhao Liu [1], Hongyu Yi [1], Dapeng Gu [2,*] and Xingang Liu [2]

[1] National Engineering Research Center for Advanced Manufacturing Technology and Equipment of Heavy Castings and Forgings, Erzhong (Deyang) Heavy Equipment Co., Ltd., Deyang 618013, China; maochuanghit@126.com (C.M.); sun_luo@126.com (L.S.); 13689621756@163.com (J.L.); yi_hy337@163.com (H.Y.)
[2] School of Mechanical Engineering, Yanshan University, Qinhuangdao 066004, China; lmz20002023@163.com (M.L.); xinruiwang@stumail.ysu.edu.cn (X.W.); lxg@ysu.edu.cn (X.L.)
[3] Sinomach Heavy Equipment Group Co., Ltd., Deyang 618000, China; renlanjun@sinomach-he.cn
* Correspondence: jsgudapeng@ysu.edu.cn; Tel.: +86-0335-8057031

Abstract

In this study, double-pass hot compression tests were conducted to systematically investigate the effects of hot deformation parameters on the static recrystallization (SRX) behavior of SA-508M Gr.3 steel used for nuclear reactor pressure vessels. The deformation temperatures were set to 950, 1050, and 1150 °C, with strain rates of 0.01, 0.1, and 1 s^{-1}. The first-pass strains were 0.05, 0.10, and 0.15; the inter-pass time was fixed at 60 s; and the second-pass strain was maintained at 0.05. Based on the experimental data, a kinetic model describing SRX softening behavior was established. The activation energy for SRX was determined to be 81.45 kJ·mol^{-1}, and the Avrami exponent was 0.5742. The characteristic time for 50% recrystallization ($t_{0.5}$) was quantified under different deformation conditions. In addition, the microstructural evolution of SRX after double-pass hot compression was characterized using electron backscatter diffraction (EBSD). The results show that increasing the deformation temperature and strain rate leads to opposite trends in the flow stress during double-pass deformation, with the flow stress decreasing with temperature and increasing with strain rate. Meanwhile, inter-pass static softening is enhanced, resulting in a pronounced stress drop during the second pass. An increase in the first-pass strain further intensifies the stress drop and enhances the extent of SRX. EBSD analysis reveals consistent microstructural evolution: with increasing deformation temperature, strain rate, and the first-pass strain, the misorientation distribution shifts from low-angle grain boundaries (LAGBs) to high-angle grain boundaries (HAGBs), indicating an increased degree of SRX. These findings provide a theoretical basis and experimental support for process parameter optimization and engineering applications of SA-508M Gr.3 steel.

Keywords: SA-508M Gr.3 steel; static recrystallization (SRX) behavior; microstructure evolution; double-pass hot compression

Check for updates

Academic Editor: Andrea Di Schino

Received: 28 May 2026
Revised: 15 June 2026
Accepted: 19 June 2026
Published: 25 June 2026

Copyright: © 2026 by the authors. Licensee MDPI, Basel, Switzerland. This article is an open access article distributed under the terms and conditions of the Creative Commons Attribution (CC BY) license.

1. Introduction

SA-508M Gr.3 steel is widely used in critical components such as nuclear reactor pressure vessels due to its excellent strength and toughness [1]. SA-508/SA-508M Grade 3 (including modified variants reported as SA-508M Gr.3) is specified for quenched-and-tempered vacuum-treated pressure vessel forgings in relevant codes and standards [2].

With the continuous development of nuclear power infrastructure at home and abroad, understanding the hot-deformation behavior and inter-pass static recrystallization of reactor pressure vessel steels, such as SA-508M Gr.3, is of increasing industrial significance. Its service safety and reliability impose stringent requirements on material microstructural uniformity [3,4]. SA-508M Gr.3 steel typically undergoes multi-pass deformation during hot working processes, thereby triggering the static recrystallization (SRX) softening mechanism between passes [5,6]. The occurrence of SRX significantly influences the grain refinement and microstructural homogeneity [7,8]. Therefore, in-depth investigation of the SRX behavior and microstructure evolution of SA-508M Gr.3 steel holds important theoretical significance and engineering value.

Numerous studies have been conducted by researchers on the SRX behavior of alloy steels. For instance, recent double-pass hot compression studies on non-SA508 steels also established Avrami-type SRX kinetic models and reported diffusion-range apparent activation energies, further supporting the generality of this methodology [9]. Li et al. [10] performed double-pass isothermal hot compression experiments on low-carbon bainitic steel and established a SRX kinetic equation, quantitatively revealing the relationship between the softening fraction and the strain rate, deformation temperature, and inter-pass time. Similarly, Xu et al. [11] conducted double-pass hot compression tests on 12Cr ultra-supercritical rotor steel, systematically studied the static softening behavior during SRX, and developed and modified an SRX kinetic model for predicting the recrystallization fraction and softening degree. Based on dislocation density theory, Yang et al. [12] employed a mesoscopic cellular automaton model to investigate the microstructural evolution of SRX during isothermal treatment of solid-state bonded joints in SA508-3 steel. The results indicated that temperature dominates the recrystallization and grain size/morphology evolution and significantly enhances the interfacial bonding ratio, while the influence of pre-strain is relatively weak. The model-predicted average grain size agreed well with experimental data and can be used to quantitatively evaluate the bonding quality.

It is noteworthy that process parameters such as deformation temperature, strain rate, and inter-pass time are key factors influencing SRX behavior [13,14]. These parameters not only determine the initiation and progression of SRX softening but also directly relate to the appropriate selection of physical parameters in actual forging processes [15]. Therefore, based on the requirements of industrial hot forming processes, Dong et al. [16] systematically investigated the effects of the deformation temperature, strain rate, pre-strain, initial austenite grain size, and inter-pass time on the SRX softening kinetics of SA508-3 steel through isothermal double-pass hot compression tests. Furthermore, they established a kinetic evolution model capable of predicting softening behavior and static recrystallized grain size, providing a basis for process parameter optimization.

Although Dong et al. systematically investigated the SRX behavior of SA508-III steel during hot deformation and established kinetic models for static softening and recrystallized grain size, further understanding is still required regarding the correlation between inter-pass softening behavior and microstructural evolution in SA-508M Gr.3 steel under different deformation parameters. In particular, the evolution of grain-boundary misorientation, the transition from low-angle grain boundaries (LAGBs) to high-angle grain boundaries (HAGBs), and the role of relatively small first-pass strains in the competition between static recovery and SRX have not been sufficiently clarified. Therefore, the present work aims to complement previous studies by combining double-pass hot compression tests with EBSD characterization to investigate the SRX kinetics and microstructural evolution of SA-508M Gr.3 steel. The specific contributions of this study include (i) establishing an apparent SRX kinetic model under the present double-pass hot compression conditions; (ii) correlating the calculated inter-pass softening fraction with EBSD-based misorientation

evolution; and (iii) clarifying the effects of the deformation temperature, strain rate, first-pass strain, and inter-pass time on the LAGB-to-HAGB transition and SRX development.

2. Experimental Materials and Methods

To simulate the thermo-mechanical history of multi-pass hot working and to quantify inter-pass softening in SA-508M Gr.3 steel, double-pass hot compression tests were designed and conducted as described below. This testing method was selected because it reproduces the typical deformation–inter-pass holding–re-deformation sequence during multi-pass hot forging and enables the quantitative evaluation of inter-pass static softening and SRX kinetics in SA-508M Gr.3 steel.

Materials and Experimental Procedure

The experimental SA-508M Gr.3 steel used in this study was provided by Erzhong (Deyang) Heavy Equipment Co., Ltd. The chemical composition of SA-508M Gr.3 steel is presented in Table 1. The specimen was machined into a cylinder with a diameter of 8 mm and a height of 12 mm.

Table 1. Chemical composition of SA-508M Gr.3 steel (wt.%).

C	Si	Mn	Cr	Mo	Ni	Al	Fe
0.17	0.20	1.42	0.20	0.46	0.77	0.02	Bal.

The initial microstructure of SA-508M Gr.3 steel before hot compression is shown in Figure 1a. The microstructure consisted of equiaxed grains with an average grain size of approximately 208 μm, which served as the initial condition for the subsequent double-pass hot compression experiments. Figure 1b shows a schematic of the double-pass hot compression process. The specific parameters of the double-pass hot compression are provided in Table 2. The hot compressed specimens were heated to 1200 °C at a constant rate of 10 °C/s and held for 180 s to ensure the uniformity of their initial states. Then, the specimens were cooled at a rate of 10 °C/s to the deformation temperature T_1 of the first-pass hot compression and held for 60 s. The first-pass hot compression was performed at the specified deformation temperature T_1, strain rate $\dot{\varepsilon}_1$, and strain ε_1. After the first pass of deformation, the sample was insulated at a specific interval time t by using the automatic temperature control system of the thermal simulator, and no additional mechanical load was applied during the holding period between passes. Then, the second-pass hot compression was performed at the specified deformation temperature T_2, strain rate $\dot{\varepsilon}_2$, and strain ε_2. The specimens subjected to the double-pass hot compression were immediately water-cooled to room temperature. In addition, to mitigate friction effects during compression, mica sheets were placed between the specimen end faces and the anvils prior to deformation. In addition, metallic pads were applied to reduce the heat loss at the specimen ends, thereby minimizing the end-surface cooling during the tests.

The conversion rate of SA-508M Gr.3 steel was calculated using the 0.2% offset stress method based on the real stress–strain curve [17]. The volume fraction of SRX (X_{SRX}) can be obtained from the following equation:

$$X_{SRX} \approx F_s = (\sigma_m - \sigma_2)/(\sigma_m - \sigma_1) \quad (1)$$

where F_s is the SRX softening rate; σ_m is the flow stress at the end of the first stage deformation; and σ_1 and σ_2 are the 0.2% offset stresses after the first- and second-stage deformation, respectively.

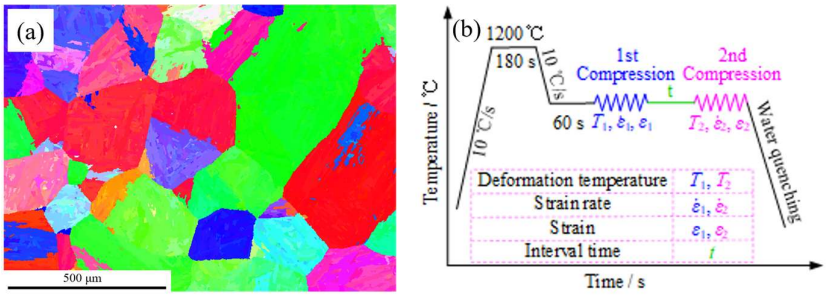


Figure 1. The double-pass hot compression experiment: (**a**) the IPF diagram of the sample before compression, (**b**) the schematic diagram of the experimental process.

Table 2. Process parameters of the double-pass hot compression.

No.	The First-Pass Hot Compression			Interval Time *t*/s	The Second-Pass Hot Compression		
	T_1/°C	$\dot{\varepsilon}_1$/s^{-1}	ε_1		T_2/°C	$\dot{\varepsilon}_1$/s^{-1}	ε_2
1	950	0.1	0.10	30, 60, 90, 150	950	0.1	0.05
2	1050	0.1	0.10	10, 30, 60, 90	1050	0.1	0.05
3	1150	0.1	0.10	10, 30, 60, 90	1150	0.1	0.05
4	1050	0.01	0.10	5, 10, 30, 60	1050	0.01	0.05
5	1050	1	0.10	5, 10, 30, 60	1050	1	0.05
6	1050	0.01	0.05	30, 60, 90, 150	1050	0.01	0.05
7	1050	0.01	0.15	5, 10, 30, 60	1050	0.01	0.05

Electron backscatter diffraction (EBSD) characterization was performed using a field-emission scanning electron microscope (Zeiss Sigma 300, Jena, Germany) to reveal the microstructural features. The measurements were conducted with an accelerating voltage of 20 kV, a working distance of 18 mm, and a step size of 0.5 μm. The data were subsequently analyzed using AZtecCrystal 3.2 software, in which grain boundaries with misorientation angles of 2–15° were defined as low-angle grain boundaries (LAGBs), and those with misorientation angles greater than 15° were defined as high-angle grain boundaries (HAGBs). The samples were subjected to final OPS polishing to remove the surface deformation layer and ensure high-quality EBSD diffraction patterns.

3. Results and Discussion

3.1. Flow Curves for Double-Pass Hot Compression

Based on the experimental protocol outlined in Section 2, the flow curves under different temperatures, strain rates, inter-pass times, and first-pass strains are presented first to provide the basis for the subsequent softening analysis and SRX kinetics modeling. Figure 2 presents the double-pass hot compression flow stress curves of SA-508M Gr.3 steel under different deformation conditions of inter-pass time, deformation temperature, strain rate, and the first-pass strain. As illustrated in Figure 2a, the flow stress curve of the first pass is basically similar. Under the condition that other parameters remain unchanged, the flow stress curve of the second pass shows a significant "stress drop" compared with the flow stress curve of the first pass, meaning that the stress of the second pass is lower than the stress at the end of the first pass. The degree of "stress drop" in the second pass of flow stress gradually increases as the interval time extends from 5 s to 90 s. This phenomenon is attributed to the static recovery and SRX processes that occur within SA-508M Gr.3 steel during the interval period of the double-pass hot compression. The effect of SRX becomes increasingly dominant with a prolonged pass interval time, thereby partially or completely eliminating the work-hardening effect caused by the first-pass deformation. As shown

in Figure 2b, as the deformation temperature increases, the flow stresses of both the first and second passes decrease. It also indicates that the increase in temperature promotes static softening behavior during the interval between the first pass and the second pass. Thus, the increase in temperature leads to a substantial reduction in the flow stress during the second pass with the increase in the deformation temperature. In Figure 2c, as the strain rate increases, the flow stresses of both the first and second passes increase. This is attributed to the fact that high strain rates result in a rapid accumulation of dislocation density and a greater amount of stored distortional energy within the material, inducing a pronounced increase in work hardening. Furthermore, a high dislocation density and more distortion energy provide more opportunities for the nucleation and growth rate of SRX. In Figure 2d, under the present experimental conditions, when the strain of the first pass is 0.05, the flow stress curve of the second pass appears as a natural extension of the first-pass curve, without an obvious "stress drop". This absence may be attributed to the relatively small first-pass strain, which introduces limited dislocation density and stored deformation energy. Under the present experimental conditions, ε_1 = 0.05 appears to be insufficient to induce appreciable SRX during the inter-pass interval, and the inter-pass softening is likely dominated by static recovery. Therefore, the SRX degree at ε_1 = 0.05 is limited compared with those at higher first-pass strains. When the strain of the first pass is increased to 0.1 and 0.15, the flow stress curve of the second pass exhibited a discernible "stress drop" relative to that of the first pass. This phenomenon signifies that a strain of 0.1 in the first pass exceeds the critical strain for SRX, confirming that SRX has been initiated. And the larger the strain of the first pass, the more complete the SRX, which, in turn, leads to a greater degree of "stress drop".

The variation in X_{SRX} (F_s) with inter-pass time under different deformation process parameters is shown in Figure 3. As shown in Figure 3a–c, X_{SRX} (F_s) exhibits a consistent trend of increasing with the inter-pass time across all tested deformation process parameters. The kinetics are characterized by a rapid SRX rate within the first 60 s, followed by a noticeable deceleration thereafter. Under constant deformation conditions, X_{SRX} (F_s) exhibits a positive correlation with key processing parameters: deformation temperature (Figure 3a), strain rate (Figure 3b), and the first-pass strain (Figure 3c). The enhancement of these parameters collectively accelerates the recrystallization kinetics, which is evidenced by a distinct upward and leftward shift in the X_{SRX} (F_s) versus inter-pass time curve. Based on the analysis of Figure 2d above, it can be seen that under condition of $T_1 = T_2$ = 1050 °C, ε_1 = 0.1, ε_2 = 0.05, and $\dot{\varepsilon}_1 = \dot{\varepsilon}_2$ = 0.05, X_{SRX} (F_s) is about 26%. It shows that static recovery plays a leading role in inter-pass softening. SRX becomes the main softening mechanism at higher temperature, higher strain rate or larger first-pass strain.

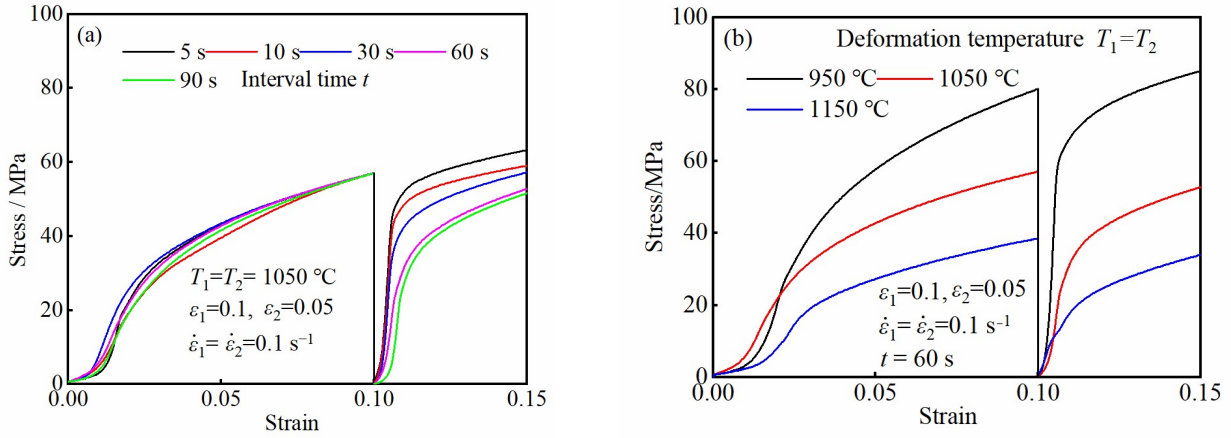


Figure 2. *Cont.*

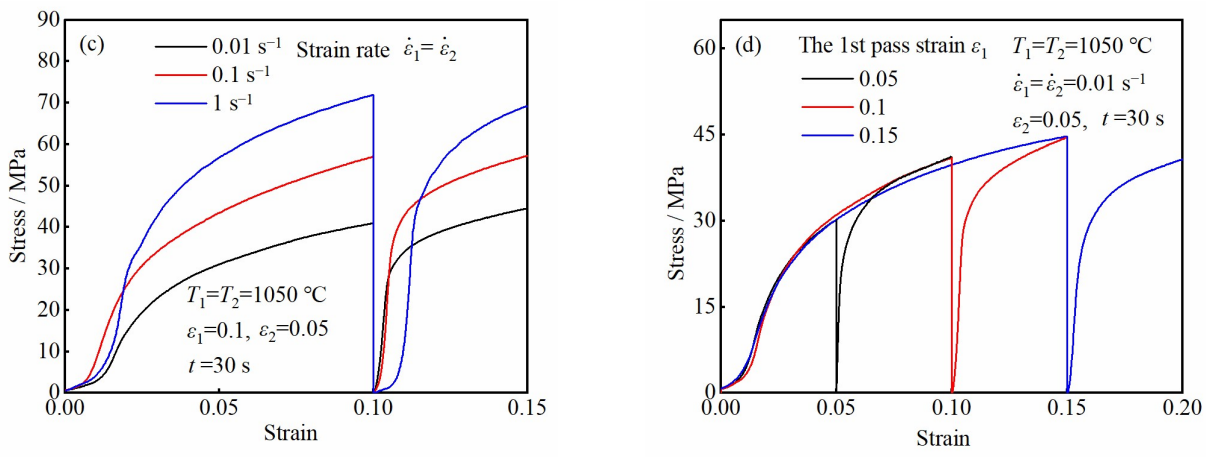


Figure 2. The stress–strain curve of double-pass hot compression under different deformation process parameters: (**a**) inter-pass time, (**b**) deformation temperature, (**c**) strain rate, and (**d**) the first-pass strain.

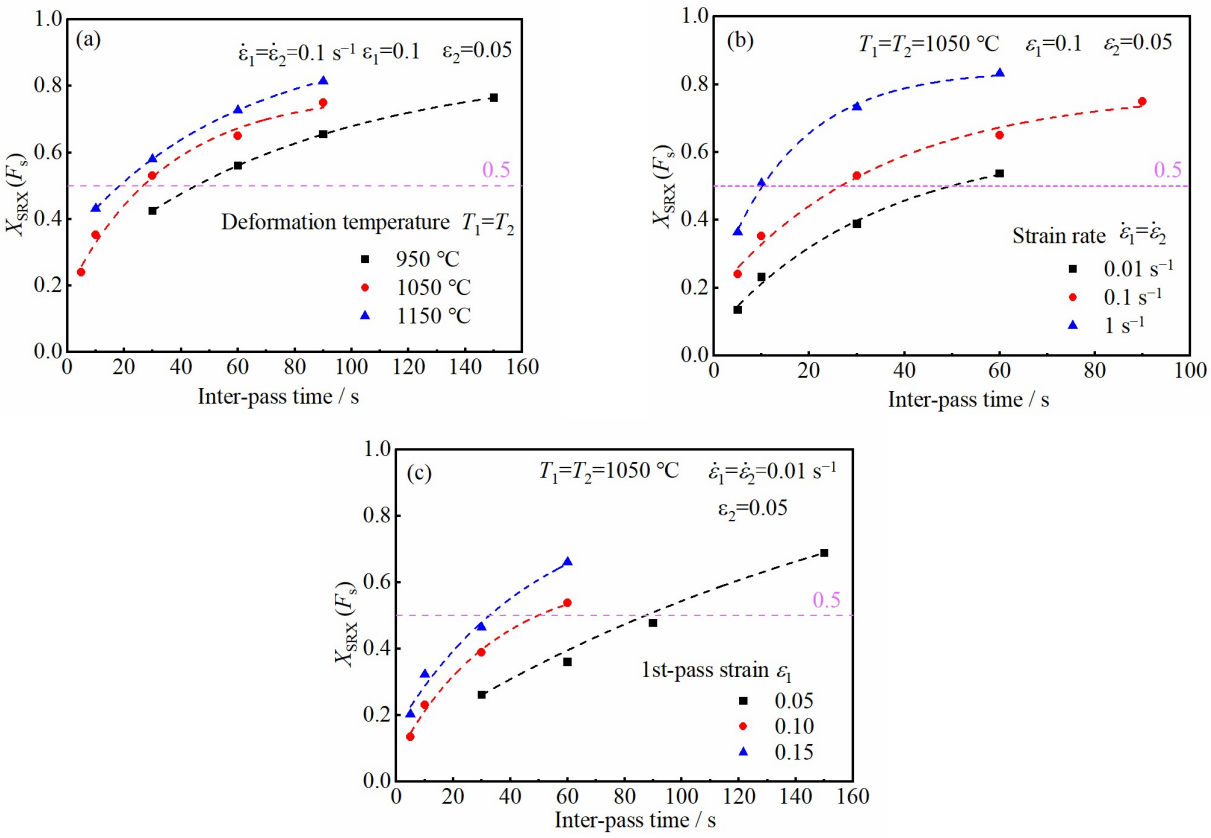


Figure 3. The effects of different parameters on the volume fraction of SRX in SA-508M Gr.3 steel: (**a**) deformation temperature, (**b**) strain rate, and (**c**) first-pass strain.

3.2. The Kinetics of SRX

The classic Avrami equation was used to describe the SRX dynamics of SA-508M Gr.3 steel [18,19]:

$$X_{SRX} = 1 - \exp[-0.69(\frac{t}{t_{0.5}})^{n}] \quad (2)$$

where X_{SRX} is the volume fraction of SRX; n is the materials constant; and $t_{0.5}$ is the time when the SRX volume fraction reaches 50%, which can be described as

$$t_{0.5} = B\varepsilon^{b_1}\dot{\varepsilon}^{b_2}\exp\left(\frac{Q_S}{RT}\right) \tag{3}$$

where B, b_1 and b_2 are the material constants, ε is the strain, $\dot{\varepsilon}$ is the strain rate, R is the gas constant (J/mol·k), T is the absolute temperature (K), and Q_S is the SRX activation energy (kJ/mol).

To establish the SRX kinetics model for SA-508M Gr.3 steel, taking the logarithm of both ends of Equation (2) yields

$$\ln\left(\ln\frac{1}{1-X_{SRX}}\right) = \ln 0.69 + n(\ln t - \ln t_{0.5}) \tag{4}$$

$t_{0.5}$ can be obtained from Figure 3, and a linear fit can be applied to $(\ln t - \ln t_{0.5})$ versus $\ln\{\ln[1/(1-X_{SRX})]\}$; as shown in Figure 4, the slope of the fitted line is n = 0.5742.

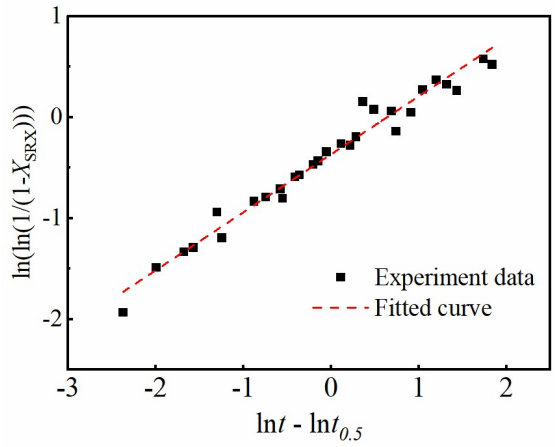


Figure 4. The fitted line of $(\ln t - \ln t_{0.5})$ and $\ln\{\ln[1/(1-X_{SRX})]\}$.

Taking the logarithm of both sides of Equation (3) gives

$$\ln t_{0.5} = \ln B + b_1 \ln\varepsilon + b_2 \ln\dot{\varepsilon} + \frac{Q_S}{RT} \tag{5}$$

Linear regression was performed on $\ln\varepsilon$ versus $\ln\varepsilon_{0.5}$, $\ln\dot{\varepsilon}$ versus $\ln\varepsilon_{0.5}$, and $1000/T$ versus $\ln\varepsilon_{0.5}$. As shown in Figure 5, the values of B, b_1, b_2, and Q_s were obtained as being 0.000731, −0.9491, −0.3528, and 81,452 J/mol, respectively. The activation energy obtained in this work is an apparent SRX value under double-pass hot deformation conditions and should not be directly equated to the lattice self-diffusion activation energy of austenite. Compared with the SRX activation energy reported for SA508Gr.4N reactor pressure vessel steel (approximately 264.23 kJ·mol^{-1}), the present value is relatively low. This discrepancy may be related to differences in chemical composition, initial austenite grain size, pre-strain range, inter-pass time, and the method used to determine the recrystallized fraction. In addition, the present activation energy was derived from the stress-softening behavior using the 0.2% offset stress method; therefore, the calculated softening fraction may include contributions from both static recovery and static recrystallization, especially under relatively small first-pass strain conditions. As a result, the obtained value should be regarded as an apparent activation energy for inter-pass static softening rather than a purely physical activation energy for complete SRX controlled only by austenite grain-boundary

migration. Similar differences in the apparent activation energy have also been reported. Therefore, the kinetics model of SRX could be described as

$$X_{SRX} = 1 - \exp\left[-0.69\left(\frac{t}{t_{0.5}}\right)^{0.5742}\right] \quad (6)$$

$$t_{0.5} = 0.000731\varepsilon^{-0.9491}\dot{\varepsilon}^{-0.3528}\exp\left(\frac{81452}{RT}\right) \quad (7)$$

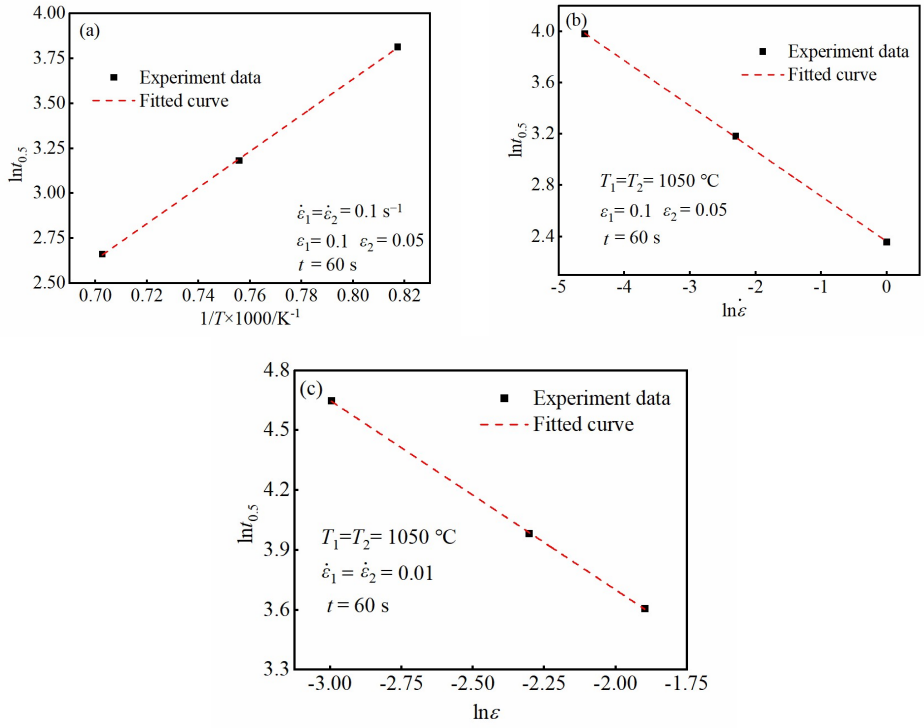


Figure 5. Fitting curve of deformation parameters and lnt0.5. (**a**) deformation temperature, (**b**) strain rate, and (**c**) the first-pass strain.

The reliability of the proposed kinetic model was further evaluated by comparing the experimentally calculated apparent SRX fractions with the model-predicted values (Figure 6). The statistical indicators were calculated to be as follows: Pearson's correlation coefficient R = 0.9829, coefficient of determination R^2 = 0.9646, average absolute relative error AARE = 4.99%, and root-mean-square error RMSE = 0.0360. These results indicate that the proposed model can reasonably describe the apparent SRX/static-softening behavior of SA-508M Gr.3 steel within the investigated deformation parameter range.

3.3. The Influence of Deformation Process Parameters on Static Softening Behavior

Figure 7 shows the EBSD characterization of SA-508M Gr.3 steel after the double-pass hot compression at the first-pass strain of 0.1; strain rate of 0.1 s^{-1}; inter-pass time of 60 s; and deformation temperatures of 950 °C, 1050 °C, and 1150 °C. SRX is a typical thermally activated process. The reconstruction of prior austenite grains from the martensitic microstructure was carried out using AZtec Crystal (Figure 7(a_1–a_3)). Meanwhile, the grain boundary characteristics of the reconstructed prior austenite grains including the fraction of low-angle grain boundaries (LAGBs) and high-angle grain boundaries (HAGBs), as well as the misorientation distribution were quantitatively analyzed. The same processing methodology was subsequently applied to the data presented in Figures 7 and 8. As the deformation temperature increases, dislocation activity is enhanced, grain boundary

migration becomes more pronounced, and the nucleation and growth rates of SRX are significantly accelerated [20]. This evolutionary behavior is further confirmed by the misorientation distribution. Specifically, as the deformation temperature increases from 950 °C to 1150 °C, the grain boundary character gradually shifts from low-angle to high-angle boundaries. The proportion of low-angle grain boundaries (LAGBs, 2–15°) decreases (from 88.5% to 83.4%) progressively, whereas the fraction of high-angle grain boundaries (HAGBs, >15°) increases (from 11.5% to 16.6%) markedly. This transition indicates a continuous enhancement in the extent of SRX with increasing temperature, which is consistent with previously reported results [21].

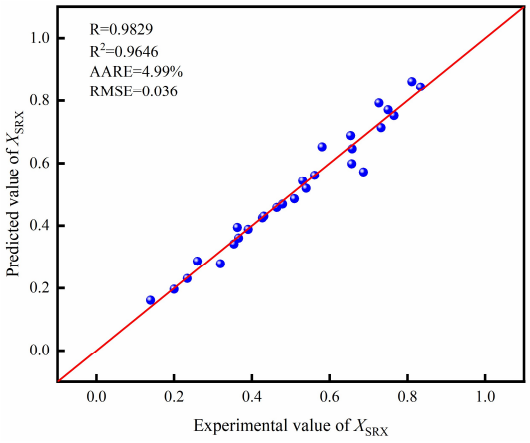


Figure 6. Comparison of X_{SRX} predicted values and experimental values under all deformation conditions and model accuracy indicators.

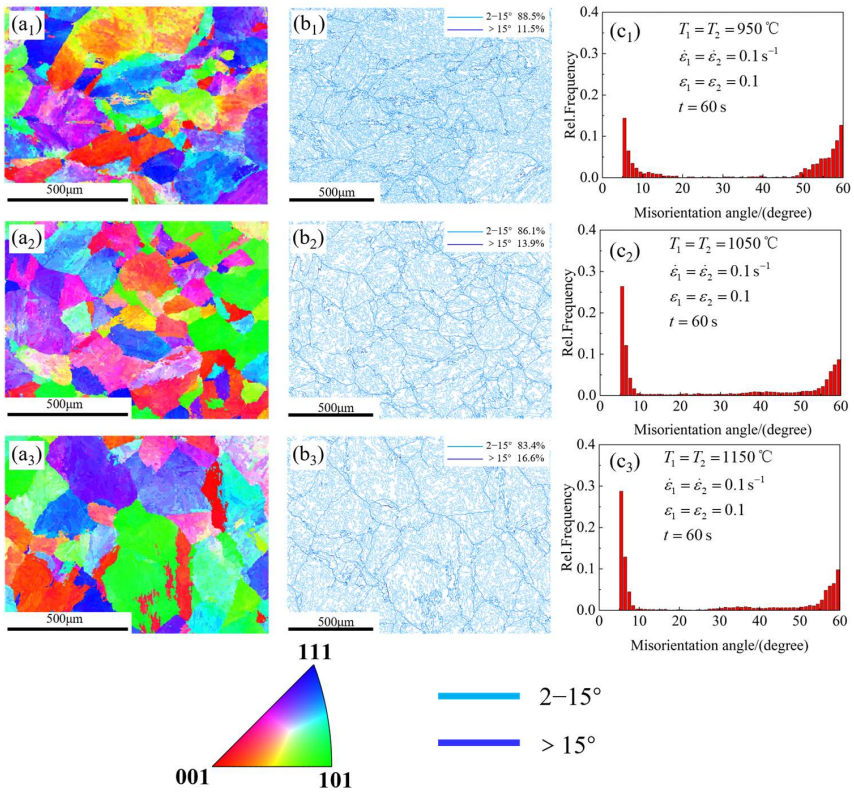


Figure 7. The EBSD characterization of SA-508M Gr.3 steel after the double-pass hot compression under deformation temperatures of 950 °C (**a1**,**b1**,**c1**), 1050 °C (**a2**,**b2**,**c2**), and 1150 °C (**a3**,**b3**,**c3**). (**a1**–**a3**) IPF after parent phase reconstruction, (**b1**–**b3**) BC (backscattered electron contrast) + GBs (grain boundaries), and (**c1**–**c3**) orientation difference distribution diagram.

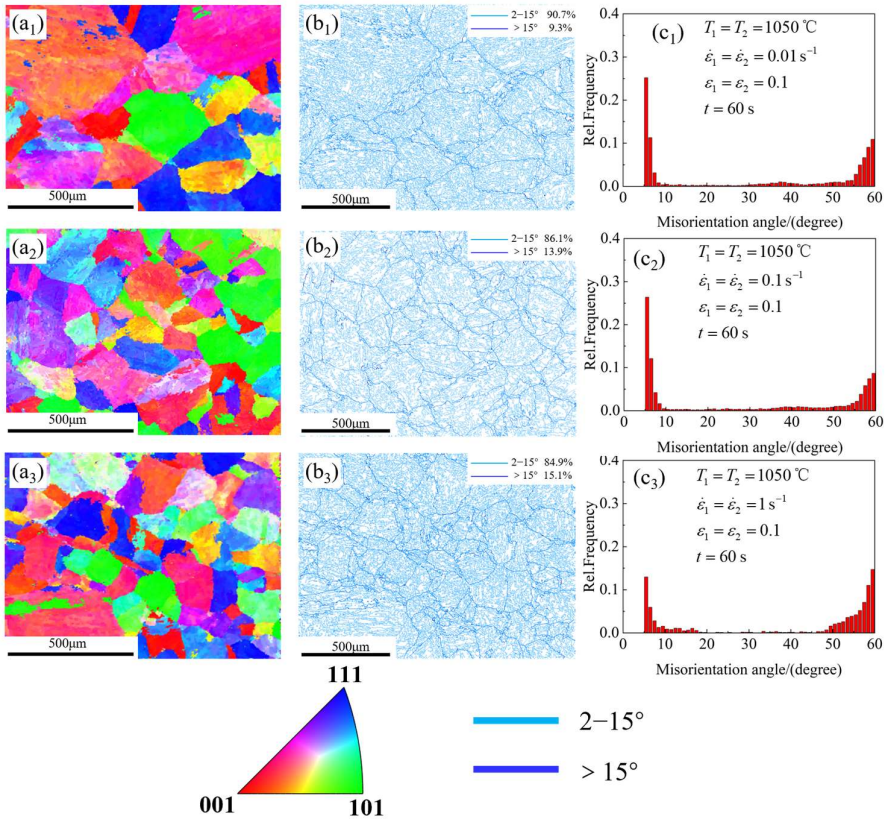


Figure 8. The EBSD characterization of SA-508M Gr.3 steel after the double-pass hot compression at strain rates of 0.01 s^{-1} (**a1**,**b1**,**c1**), 0.1 s^{-1} (**a2**,**b2**,**c2**), and 1 s^{-1} (**a3**,**b3**,**c3**). (**a1**–**a3**) IPF after parent phase reconstruction, (**b1**–**b3**) BC (backscattered electron contrast) + GBs (grain boundaries), and (**c1**–**c3**) orientation difference distribution diagram.

At a deformation temperature of 950 °C, the extent of SRX is relatively low, and the microstructure retains pronounced deformation characteristics (Figure 7(a_1)). The corresponding misorientation angle distribution is dominated by LAGBs, with a relatively small fraction of HAGBs. As the deformation temperature increases to 1050 °C, the proportion of LAGBs decreases markedly, while that of HAGBs increases significantly, indicating an enhanced degree of SRX. At this temperature, HAGBs and re-crystallized grain boundaries are more fully developed, and the grain structure becomes increasingly uniform (Figure 7(b_1)). When the deformation temperature is further raised to 1150 °C, the EBSD misorientation distribution continues to shift toward higher angles, and the fraction of HAGBs reaches its maximum. This suggests that the material is in a highly softened state prior to the second-pass deformation, with SRX approaching completion at 1150 °C. This interpretation is supported by the EBSD features typical of a near-fully recrystallized microstructure, including predominantly equiaxed grains, the high HAGB fraction, and the overall shift of the misorientation distribution toward higher angles. Consequently, the second pass exhibits characteristics of "secondary deformation after recrystallization" [20]. In addition, the higher deformation temperature significantly enhances the grain boundary mobility and promotes the rapid growth of recrystallized grains, leading to an increase in the average grain size (Figure 7(a_3)), increased from 226 μm to 293 μm.

In addition, the increase in X_{SRX} observed in Figure 3 is generally consistent with the evolution of grain boundary characteristics shown in Figure 7. Specifically, the increase in HAGB fraction is qualitatively consistent with the increase in the apparent SRX/static-softening fraction calculated from the flow-stress data, indicating that the EBSD results provide microstructural support for the softening trend rather than a direct one-to-one

quantitative measurement of the SRX fraction. Similar consistency can also be observed in Figures 8 and 9.

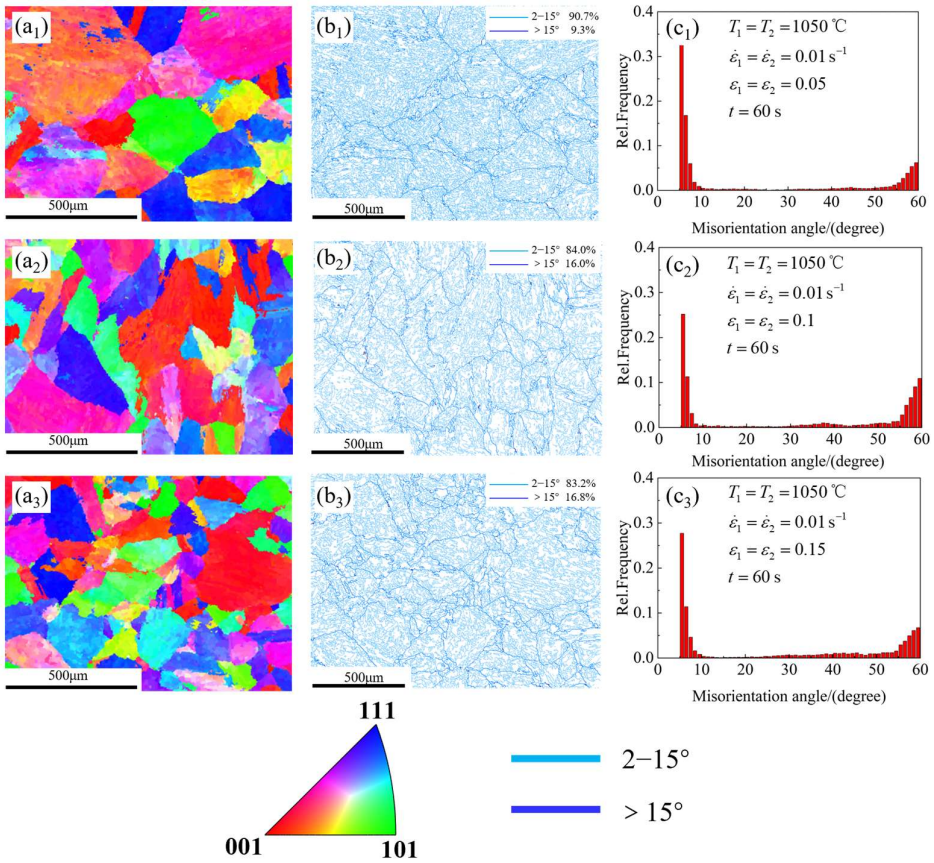


Figure 9. The EBSD characterization of SA-508M Gr.3 steel after the double-pass hot compression with the first-pass strains of 0.05 (**a1**,**b1**,**c1**), 0.1 (**a2**,**b2**,**c2**), and 0.15 (**a3**,**b3**,**c3**). (**a1**–**a3**) IPF after parent phase reconstruction, (**b1**–**b3**) BC (backscattered electron contrast) + GBs (grain boundaries), and (**c1**–**c3**) orientation difference distribution diagram.

Figure 8 shows the EBSD characterization of SA-508M Gr.3 steel after the double-pass hot compression at the first-pass strain of 0.1; deformation temperature of 1050 °C; inter-pass time of 60 s; and strain rates of 0.01 s^{-1}, 0.1 s^{-1}, and 1 s^{-1}. The results demonstrate that an increase in the strain rate accelerates the dislocation accumulation during deformation and enhances the storage of deformation energy, thereby providing a greater internal driving force for SRX during the inter-pass interval [22]. This promotes the nucleation and growth of recrystallized grains and leads to an increased extent of SRX within the same inter-pass time. Correspondingly, the EBSD misorientation distributions exhibit an evolutionary trend similar to that observed with increasing deformation temperature. With increasing strain rate, the grain boundary character shifts from low-angle to high-angle boundaries, as evidenced by a decrease in the fraction of LAGBs (from 90.7% to 84.9%) and a concomitant increase in HAGBs (from 9.3% to 15.1%), indicating an enhanced degree of SRX.

At a strain rate of 0.01 s^{-1}, the EBSD misorientation distribution is dominated by LAGBs, with a relatively small fraction of HAGBs. Owing to the prolonged deformation time, static recovery after deformation is more pronounced, leading to the consumption of stored deformation energy. Consequently, the driving force for SRX is insufficient, resulting in limited formation of recrystallized grain boundaries and the retention of a large number of subgrain structures in the microstructure. When the strain rate is increased to 0.1 s^{-1}, the shortened deformation time suppresses dislocation recovery, leading to a significant

increase in the dislocation density and stored deformation energy after deformation. This enhances the internal driving force for SRX during the inter-pass interval, facilitating more extensive and easier nucleation of recrystallized grains and promoting microstructural homogenization. Accordingly, the misorientation distribution shifts toward higher angles, with a marked increase in the fraction of HAGBs and a corresponding decrease in LAGBs. Upon further increasing the strain rate to 1 s^{-1}, the stored deformation energy after deformation reaches its maximum, resulting in more fully developed recrystallized grain boundaries and a higher proportion of HAGBs. Consequently, SRX is initiated more rapidly and proceeds more thoroughly. Therefore, the effect of strain rate on SRX in SA-508M Gr.3 steel should be interpreted as the combined result of stored deformation energy, recovery behavior, and inter-pass recrystallization kinetics. Under the present experimental conditions, increasing the strain rate generally promotes SRX, as evidenced by the higher HAGB fraction and the shift in the misorientation distribution toward higher angles.

Figure 9 shows the EBSD characterization of SA-508M Gr.3 steel after the double-pass hot compression at the deformation temperatures of 1050 °C; strain rate of 0.1 s^{-1}; inter-pass time of 60 s; and the first-pass strains of 0.05, 0.1, and 0.15. As the first-pass strain increases, the introduced dislocation density and stored deformation energy increase accordingly, providing a greater driving force for the nucleation and growth of SRX during the inter-pass interval, thereby facilitating recrystallization [23]. The misorientation distributions further corroborate this evolution of SRX, showing that a higher first-pass strain induces a greater extent of SRX and promotes a more pronounced transition from low-angle to high-angle grain boundaries. When the first-pass strain is 0.05, the stored deformation energy is relatively low, and static recovery dominates during the inter-pass interval, resulting in a limited extent of SRX. Consequently, grain growth is more likely to occur during the high-temperature inter-pass holding period, leading to a relatively coarse grain structure. As the first-pass strain increases to 0.10, the stored deformation energy increases, promoting more extensive nucleation and growth of SRX, which results in a more equiaxed and homogeneous grain structure. Correspondingly, the misorientation distribution exhibits a decrease in the fraction of LAGBs (from 90.7% to 83.2%) and an increase in HAGBs (from 9.3% to 16.8%). With a further increase in the first-pass strain to 0.15, the driving force for SRX is further enhanced, leading to a more complete recrystallization process and a continued shift of the misorientation distribution toward higher angles, with a higher proportion of HAGBs. In other words, the evolution shifts from an SRX-dominated stage to a post-recrystallization grain-growth-dominated stage at $\varepsilon_1 = 0.15$. Notably, the grain size under this condition is larger than that at a strain of 0.10, suggesting that SRX is completed earlier during the inter-pass interval, thereby allowing grain growth to occur in the later stage and resulting in a certain degree of grain coarsening. Similar findings were also reported by Xu et al. [13] in their study on the double-stage hot deformation of 7Mo super-austenitic stainless steel, where the deformation temperature, first-stage strain, and strain rate were shown to strongly influence SRX behavior. More importantly, their work emphasized the important roles of stored deformation energy, grain boundary evolution, and recrystallization nucleation mechanisms during inter-pass holding, which is consistent with the LAGB-to-HAGB transition observed in the present study.

4. Conclusions

In this study, double-pass hot compression tests were conducted to systematically investigate the SRX behavior and microstructural evolution of SA-508M Gr.3 steel under varying deformation temperatures (950, 1050, and 1150 °C), strain rates (0.01, 0.1, and 1 s^{-1}), and the first-pass strains (0.05, 0.10, and 0.15). The main conclusions are summarized as follows:

1. With increasing deformation temperature, the flow stress decreases and inter-pass static softening becomes more pronounced, making the occurrence of stress drops in the second pass more evident. As the strain rate increases, the flow stress rises due to the rapid accumulation of dislocations and the associated increase in stored energy, while stress drops are likewise observed in the second pass. With increasing first-pass strain, the stress drop in the second pass becomes progressively more pronounced. When the first-pass strain is 0.05, almost no obvious stress drop is observed in the second-pass flow curve, suggesting that the stored deformation energy is insufficient to induce appreciable SRX and that static recovery dominates the inter-pass softening under the present conditions. At first-pass strains of 0.10 and 0.15, distinct stress drops appear, indicating the progressive development of SRX with increasing first-pass strain.
2. Based on the stress–strain data obtained from the flow curves, the SRX kinetics of SA-508M Gr.3 steel were described using the Avrami model. The activation energy for SRX during double-pass hot compression was determined to be 81,452 J·mol^{-1}. Accordingly, the SRX kinetic model for SA-508M Gr.3 steel can be expressed as follows:

$$\begin{cases} X_{\mathrm{SRX}} = 1 - \exp\left[-0.69\left(\frac{t}{t_{0.5}}\right)^{0.5742}\right] \\ t_{0.5} = 0.000731\varepsilon^{-0.9491}\dot{\varepsilon}^{-0.3528}\exp\left(\frac{81452}{RT}\right) \end{cases}$$

The SRX kinetic parameters established under isothermal conditions (T_1 = T_2) provide a benchmark description of SRX behavior within the investigated range, and the classical JMA equation was adopted due to its robust fit to the measured X_{SRX}-t data. However, as a macroscopic fitting approach, the present model does not explicitly account for non-isothermal temperature histories, impingement, or site-saturation effects, and its applicability is therefore limited to the current experimental conditions. Future work will extend the model to industrial forging via temperature–time path integration and/or thermomechanical coupled simulations with more mechanistic refinements.

3. The EBSD results are consistent with the aforementioned findings. With increasing deformation temperature, the misorientation angle distribution shifts toward high-angle grain boundaries (HAGBs), indicating an enhanced degree of SRX approaching complete softening; however, intensified grain boundary migration at elevated temperatures also promotes recrystallized grain growth, leading to an increase in grain size. As the strain rate increases, the higher stored energy facilitates SRX nucleation and growth, resulting in a higher fraction of HAGBs. When increasing the first-pass strain from 0.05 to 0.10, the extent of SRX increases and the microstructure becomes more equiaxed and homogeneous, whereas an excessive first-pass strain (0.15) leads to the premature completion of SRX and subsequently accelerates grain growth.

It should also be noted that the present work focuses on hot-deformation-induced static recrystallization under laboratory double-pass compression conditions. During actual service, reactor pressure vessel steels are also subjected to long-term neutron irradiation, which may significantly alter their microstructure and mechanical properties. Irradiation effects are beyond the scope of the present study, and future work combining hot-deformation microstructure control with irradiation-induced degradation would be valuable for a more comprehensive assessment of SA-508M Gr.3 steel.

Author Contributions: C.M.: Resources and Funding Acquisition; M.L.: Visualization and Writing—Original Draft; L.R.: Conceptualization and Data Curation; X.W.: Validation and Investigation; L.S.: Conceptualization and Data Curation; J.L.: Conceptualization and Data Curation; H.Y.: Conceptualization and Data Curation; D.G.: Methodology and Writing—Review and Editing; X.L.:

Supervision and Funding Acquisition. All authors have read and agreed to the published version of the manuscript.

Funding: This work was supported by National Engineering Research Center for Advanced Manufacturing Technology and Equipment of Heavy Castings and Forgings (Erzhong (Deyang) Heavy Equipment Co., Ltd. (Grant No. Q2304-7)).

Institutional Review Board Statement: Not applicable.

Informed Consent Statement: Not applicable.

Data Availability Statement: The original contributions presented in this study are included in the article. Further inquiries can be directed to the corresponding author.

Conflicts of Interest: Authors Chuang Mao, Lei Sun, Jinhao Liu, Hongyu Yi, are employees of National Engineering Research Center for Advanced Manufacturing Technology and Equipment of Heavy Castings and Forgings, Erzhong (Deyang) Heavy Equipment Co., Ltd. Author Lanjun Ren are employees of Sinomach Heavy Equipment Group Co., Ltd. The remaining authors declare that the research was conducted in the absence of any commercial or financial relationships that could be construed as a potential conflict of interest.

References

1. Lee, B.S.; Kim, M.C.; Yoon, J.H.; Hong, J.H. Characterization of high strength and high toughness Ni-Mo-Cr low alloy steels for nuclear application. *Int. J. Press. Vessel. Pip.* **2010**, *87*, 74–80.
2. Ge, S.; Niu, B.; Wang, Z.-H.; Pan, Q.-F.; Liu, C.-H.; Wang, Q. Recrystallization Behavior and Mechanical Property of a Medium-Si 12%Cr Reduced Activation Ferritic/Martensitic Steel Cladding Tube During the Manufacture. *Acta Metall. Sin. (Engl. Lett.)* **2025**, *38*, 1385–1396.
3. Sun, M.; Hao, L.; Li, S.; Li, D. Modeling flow stress constitutive behavior of SA508-3 steel for nuclear reactor pressure vessels. *J. Nucl. Mater.* **2011**, *418*, 269–280. [CrossRef]
4. Tang, Z.; Huang, C.; Niu, J.; Jiang, G. The relation among the stored energy, microstructure and hardening effect of SA508-III steel under different deformation conditions. *Mater. Sci. Eng. A* **2022**, *847*, 143333. [CrossRef]
5. Baharvand, M.; Habibi Parsa, M.; Mirzadeh, H. Achieving Fine-Grained Microstructure in Low-Alloy Steel: A Study on Static Recrystallization Using Experimental and Simulation Approaches. *Steel Res. Int.* **2025**, *96*, 235–248.
6. Dehghan-Manshadi, A.; Barnett, M.R.; Hodgson, P.D. Hot deformation and recrystallization of austenitic stainless steel: Part I. Dynamic recrystallization. *Mater. Sci. Eng. A* **2008**, *39*, 1359–1370. [CrossRef]
7. Rezvani, A.; Ebrahimi, R.; Bagherpour, E. Static Recrystallization Simulation of Interstitial Free-Steel by Coupling Multi-Phase-Field and Crystal Plasticity Model Considering Dislocation Density Distribution. *Adv. Eng. Mater.* **2025**, *27*, 2500117.
8. Liu, L.; Wu, Y.; Gong, H.; Ahmad, A. Static softening behavior and modified kinetics of Al 2219 alloy based on a double-pass hot compression test. *Materials* **2020**, *13*, 3862. [CrossRef] [PubMed]
9. Yang, J.; Wang, Q.; Yang, T.; Du, Z. The dynamic and static softening mechanisms of LX82A steel in double-pass hot compression deformation. *J. Mater. Sci.* **2025**, *60*, 17829–17847.
10. Li, L.; Zheng, L.; Ye, B.; Tong, Z. Metadynamic and static recrystallization softening behavior of a bainite steel. *Met. Mater. Int.* **2018**, *24*, 60–66. [CrossRef]
11. Xu, Y.; Zhao, Y.; Liu, J. A modified kinetics model and softening behavior for static recrystallization of 12Cr ultra-super-critical rotor steel. *Mater. Res. Express* **2020**, *7*, 056507.
12. Yang, X.; Tong, D.; Gong, M.; Guo, Z. Mesoscale simulation of interfacial microstructure evolution and healing mechanism manufactured by solid state bonding for metals during isothermal treatment. *J. Mater. Res. Technol.* **2025**, *39*, 3325–3339. [CrossRef]
13. Xu, S.; He, J.; Zhang, R.; Zhang, F. Static recrystallization behaviors and mechanisms of 7Mo super-austenitic stainless steel with undissolved sigma precipitates during double-stage hot deformation. *J. Iron Steel Res. Int.* **2024**, *31*, 475–487.
14. Wang, Q.; Hu, B.; Zhao, H.; Ru, Y. Evolution of static recrystallization microstructure caused by residual strain of an Al-richen Ni-based single crystal superalloy. *Mater. Sci. Eng. A* **2024**, *894*, 146188.
15. Kim, M.C.; Park, S.G.; Lee, K.H.; Lee, B.S. Comparison of fracture properties in SA508 Gr. 3 and Gr. 4N high strength low alloy steels for advanced pressure vessel materials. *Int. J. Press. Vessel. Pip.* **2015**, *131*, 60–66.
16. Dong, D.; Chen, F.; Cui, Z. Static recrystallization behavior of SA508-III steel during hot deformation. *J. Iron Steel Res. Int.* **2016**, *23*, 466–474. [CrossRef]
17. Lan, L.Y.; Qiu, C.L.; Zhao, D.W.; Gao, X.H. Dynamic and static recrystallization behavior of low carbon high niobium microalloyed steel. *J. Iron Steel Res.* **2011**, *18*, 55–60. [CrossRef]

18. Jiang, F.; Zhang, H.; Li, L.; Chen, J. The kinetics of dynamic and static softening during multistage hot deformation of 7150 aluminum alloy. *Mater. Sci. Eng. A* **2012**, *552*, 269–275. [CrossRef]
19. Chen, F.; Sui, D.; Cui, Z. Static recrystallization of 30Cr2Ni4MoV ultra-super-critical rotor steel. *J. Mater. Eng. Perform.* **2014**, *23*, 3034–3041. [CrossRef]
20. Ghazani, M.S.; Eghbali, B. Prediction of post-deformation recrystallization kinetics in AISI 321 austenitic stainless steel using double-stage hot compression. *J. Mater. Eng. Perform.* **2019**, *28*, 3567–3575.
21. Li, Z.; Qi, Q.; Gao, Y.; Chen, H. Kinetic modeling and grain refinement mechanisms during static recrystallization of GH4169 superalloy. *Mater. Today Commun.* **2025**, *49*, 114095. [CrossRef]
22. Dong, D.; Chen, F.; Cui, Z. Investigation on metadynamic recrystallization behavior in SA508-III steel during hot deformation. *J. Manuf. Process.* **2017**, *29*, 18–28. [CrossRef]
23. Zhang, H.; Zhang, K.; Jiang, S.; Zhou, H. Dynamic recrystallization behavior of a γ'-hardened nickel-based superalloy during hot deformation. *J. Alloys Compd.* **2015**, *623*, 374–385. [CrossRef]

Disclaimer/Publisher's Note: The statements, opinions and data contained in all publications are solely those of the individual author(s) and contributor(s) and not of MDPI and/or the editor(s). MDPI and/or the editor(s) disclaim responsibility for any injury to people or property resulting from any ideas, methods, instructions or products referred to in the content.